

Multifrequency Pulsed EPR Studies of Biologically Relevant Manganese(II) Complexes

T. A. Stich¹, S. Lahiri¹, G. Yeagle¹, M. Dicus¹, M. Brynda¹, A. Gunn¹,
C. Aznar¹, V. J. DeRose², and R. D. Britt¹

¹ Department of Chemistry, University of California-Davis, Davis, California, USA

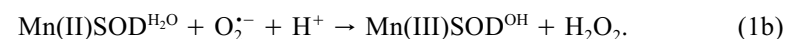
² Department of Chemistry, University of Oregon, Eugene, Oregon, USA

Received September 13, 2006; revised October 7, 2006

Abstract. Electron paramagnetic resonance studies at multiple frequencies (MF EPR) can provide detailed electronic structure descriptions of unpaired electrons in organic radicals, inorganic complexes, and metalloenzymes. Analysis of these properties aids in the assignment of the chemical environment surrounding the paramagnet and provides mechanistic insight into the chemical reactions in which these systems take part. Herein, we present results from pulsed EPR studies performed at three different frequencies (9, 31, and 130 GHz) on $[\text{Mn}(\text{II})(\text{H}_2\text{O})_6]^{2+}$, Mn(II) adducts with the nucleotides ATP and GMP, and the Mn(II)-bound form of the hammerhead ribozyme (MnHH). Through line shape analysis and interpretation of the zero-field splitting values derived from successful simulations of the corresponding continuous-wave and field-swept echo-detected spectra, these data are used to exemplify the ability of the MF EPR approach in distinguishing the nature of the first ligand sphere. A survey of recent results from pulsed EPR, as well as pulsed electron–nuclear double resonance and electron spin echo envelope modulation spectroscopic studies applied to Mn(II)-dependent systems, is also presented.

1 Mn-Containing Biological Systems

Manganese operates as a cofactor in numerous proteins, serving both catalytic and structural roles [1–4]. Many Mn-dependent enzymes take advantage of the rich redox chemistry available to the metal, accessing the +2, +3, +4, and perhaps even the +5 oxidation states during their turnover. For example, Mn-superoxide dismutase (MnSOD), which detoxifies the cell of the superoxide radical $\text{O}_2^{\cdot-}$, cycles between the Mn(II) and Mn(III) oxidation states via the ping-pong type mechanism shown below [5–9].



Other examples of such mononuclear redox-active enzymes include the manganese peroxidase responsible for lignin degradation by white-rot fungus [10–12]; a unique Mn-dependent form of lipoxygenase [13–16]; oxalate decarboxylase [17, 18]; as well as an extradiol catechol dioxygenase [19–21].

In order to help minimize kinetic and thermodynamic penalties associated with electron transfer events and the execution of chemical reactions, two or more metal centers can be coupled together to provide active sites capable of conducting multiple electrons while still operating within a physiologically accessible range of reduction potentials [22]. Only three such examples of redox-active polynuclear Mn enzymes are known: Mn-catalase that disproportionates hydrogen peroxide [23–26]; a Mn form of ribonucleotide reductase (Mn-RNR) [27, 28]; and, arguably the most recognized Mn-dependent enzyme, the photosynthetic core of green plants, algae, and certain cyanobacteria termed photosystem II (PSII) [29, 30]. Through a series of photoinitiated electron transfer events, oxidizing equivalents are stored on the tetranuclear Mn core of PSII – the oxygen-evolving complex (OEC) – which then extracts four electrons (and four protons) from two substrate water molecules to yield molecular oxygen.

In addition to the redox-active Mn-dependent enzymes described above, there exist several classes of proteins that employ one or more divalent metal ions in non-redox-active roles. Instead, these systems use the metal center in one of two ways: (i) as a Lewis acid, useful in polarizing substrate bonds for hydrolysis or in mediation of nucleophilic attack of substrate; and (ii) to stabilize tertiary structure. Such enzymes tend to be promiscuous, functioning with virtually any divalent metal ion bound in the active site. Conveniently, this allows for the substitution of electron paramagnetic resonance (EPR) silent metals such as Zn(II) and Mg(II) with the paramagnetic Mn(II) ion, thus opening avenues for a broad range of studies by EPR spectroscopy [31, 32].

Mn(II) ions also serve as a valuable probe of the Mg(II) binding sites in nucleic acids as well as catalytically relevant M^{2+} – binding sites found in nucleic acid polymerases and nucleases. A particularly interesting case is the identification and study of Mg/Mn sites in ribozymes [33]. These ions influence both folding of the RNA molecule and the catalytic activity [34]. In comparison with protein-metal binding sites, far less is known about the bonding properties and homogeneity of the metal sites in RNA. Yet as a paramagnetic substitute, Mn(II) allows detailed investigations of these properties in RNA by EPR methods [35].

In this short review, we describe first the basic theory underlying the complex spectra of Mn(II)-containing systems. Then follows a survey of the current efforts throughout the community to explore the electronic and geometric structure of these biosystems by EPR spectroscopy and the related spectroscopic techniques of electron–nuclear double resonance (ENDOR) and electron spin echo envelope modulation (ESEEM). Finally, we present results from our recent application of multifrequency, especially high-frequency, EPR spectroscopy now available at the California EPR Facility (CALEPR) in the study of aqueous Mn(II), Mn(II) coordinated by EDTA, and Mn(II)ATP and GMP complexes as models for the high-affinity metal binding site present in the hammerhead (HH)

ribozyme. Comparisons of spectral line shapes in each data set suggest unique properties for the high-affinity metal binding site in the ribozyme.

2 Spin Physics for Mn(II)

The d^5 Mn(II) ion exists in a high-spin ($S = 5/2$) ground state electron configuration in all but a few cases¹, and as such, corresponding inorganic and protein complexes are amenable to study by EPR spectroscopy. The theoretical framework that describes the origin of EPR spectra of Mn(II)-containing systems is well described elsewhere [31, 36–41] and only briefly summarized below. The energies of each spin level are understood in terms of the following effective spin Hamiltonian

$$\mathcal{H}_{\text{eff}} = \beta \vec{B}_0 \mathbf{g} \vec{S} + \vec{S} \vec{A} \vec{I} + \vec{S} \vec{D} \vec{S}. \quad (2)$$

The first term describes the Zeeman effect whereby the applied static magnetic field B_0 interacts with the unpaired electrons, breaking the Kramers degeneracy. While generally, the matrix of \mathbf{g} -values can exhibit significant anisotropy (i.e., differences from the free electron g -value = 2.0023), such is not the case for nearly all high-spin mononuclear Mn(II) systems. The five half-filled 3d-orbitals make all ligand-field excited states spin-forbidden and thus preclude spin–orbit coupling (SOC) of orbital angular momentum into the ground electronic state. Furthermore, metal-to-ligand charge transfer excited states for Mn(II) complexes are normally too high in energy and the SOC constant for the corresponding ligand atom is too small to significantly contribute to changes in \mathbf{g} . Nonetheless, with increasing magnitude of the applied magnetic field – as in a high-frequency EPR experiment – even small anisotropy (<200 ppm) in \mathbf{g} can be resolved [42]. Not affected, however, by the higher field is the hyperfine \mathbf{A} interaction between the unpaired electrons and nuclear spins. For ^{55}Mn ($I = 5/2$), this second term in Eq. (2) is manifested in the experimental spectrum by a six-fold ($2I + 1$) splitting of each EPR transition. Contributions to the \mathbf{A} -tensor values include an isotropic term A_{iso} determined by unpaired electron density localized at the nucleus and an anisotropic dipolar term A_{dip} reflecting the through-space interaction of the electron and nuclear spins. However, A_{dip} is negligible for most Mn(II) complexes due to the near spherical distribution of electron density amongst the five 3d-orbitals. In addition to the contributions from the ^{55}Mn nucleus, the hyperfine term in Eq. (2) can be expanded as a summation over all other magnetic nuclei within the vicinity of the unpaired electron, each with its own \mathbf{A} -tensor. Resolution of this “superhyperfine” interaction allows insight into the distribution of unpaired spin density about the molecule, thus

¹ Mn-phthalocyanins are known to possess an intermediate-spin quartet ground state, while Mn(II) ions in CN^- rich environments tend to be low-spin $S = 1/2$.

providing detailed structural information. Yet for Mn(II)-containing systems, these couplings tend to be small, within the line width of an EPR feature and require advanced spectroscopic techniques such as ESEEM or ENDOR to be observed [43, 44].

The final term in Eq. (2) describes the energy level splitting that occurs in the absence of an applied B field, when multiple unpaired electrons interact with each other. This term can be expanded (to first order) as a function of two empirical parameters, D and E ,

$$\tilde{S}\hat{D}\tilde{S} = D\left(\hat{S}_z^2 - \frac{S(S+1)}{3}\right) + \frac{E}{2}(\hat{S}_+^2 + \hat{S}_-^2). \quad (3)$$

These so-called zero-field splitting (ZFS) parameters are understood in terms of a crystal-field induced lowering from cubic (or higher) symmetry of the Mn(II) ion as illustrated in Fig. 1. Distortions (compressions or elongations) or significant changes in the strength of bonding along a unique molecular axis break the

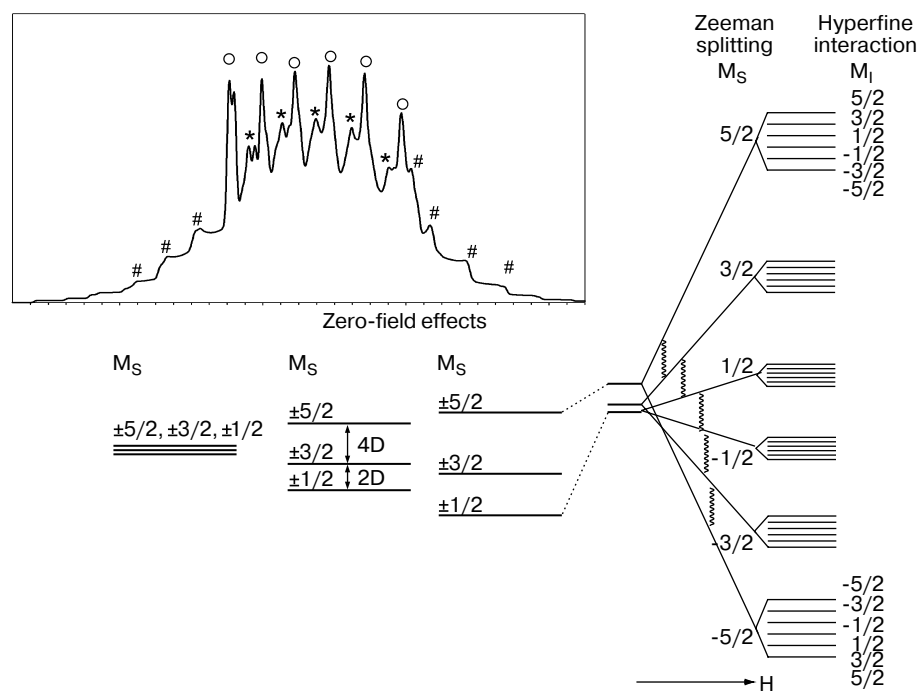


Fig. 1. Energy level diagram for the high-spin $^{55}\text{Mn(II)}$ ion ($I = 5/2$) in a spherically symmetric (left), axially distorted (center), and rhombically distorted (right) ligand field. The five rigorously allowed EPR transitions ($\Delta m_S = \pm 1$) are shown. The different classes of spectral features for a generic Mn(II)-containing system are indicated on the simulated spectrum presented in the inset. *, Forbidden transitions; O, central transitions; #, outer transitions.

degeneracy of the $m_S = |\pm 1/2\rangle, |\pm 3/2\rangle, |\pm 5/2\rangle$ Kramers doublets causing the energy of these levels to shift by Dm_S^2 , where D is known as the axial ZFS parameter (Fig. 1, center panel). Additional inequivalence in the bonding description of the equatorial ligand set induces further shifting of these energy levels by a function of E , the rhombic ZFS term (Fig. 1, right-hand side). Such rhombic distortion also mixes spin states that differ by $m_S \pm 2$, providing a mechanism for the “double quantum” transitions often observed in EPR spectra of highly distorted Mn(II) complexes [31, 45].

ZFS interactions intermix the m_l states as well, leading to the appearance of formally forbidden transitions ($\Delta m_S = \pm 1, \Delta m_l = \pm 1$) in the experimental EPR spectrum. In Mn(II) systems, such forbidden transitions manifest themselves as a set of doublets between each central transition, $|+1/2, m_l\rangle \leftrightarrow |-1/2, m_l\rangle$ (Fig. 1, inset).

Owing to the EPR selection rule $\Delta m_S = \pm 1$, inter-doublet or “outer” transitions ($|\pm 1/2\rangle \leftrightarrow |\pm 3/2\rangle$ and $|\pm 3/2\rangle \leftrightarrow |\pm 5/2\rangle$) can also be observed in perpendicular mode ($B_0 \perp B_1$) spectra. The intensity of these outer transitions is dependent in the first order on the angle between the applied magnetic field and the principal ZFS axis leading to significant broadening of these transitions for powder or frozen solution samples, whereas the manifold of central transitions remains intense as they are only perturbed by ZFS in the second order. Importantly, with respect to the outer transition intensity, any variance or strain about the ZFS values due to sample inhomogeneity prevents resolution of ^{55}Mn hyperfine features and obscures the turning points in the spectrum [46, 47].

The wave function that describes any spin system with unpaired electrons can be directly probed by EPR spectroscopy. Experimentally determined energies and intensities of transitions between spin levels report on the degree to which the $|m_S, m_l\rangle$ eigenbasis functions are mixed by ZFS and hyperfine interactions. Using the above equations, the spin Hamiltonian parameters \mathbf{g} , \mathbf{A} , D , and E can be extracted from experimental data and then related to the ligand structure surrounding the Mn(II) ion.

3 Past Studies

The diverse biological roles in which Mn takes part are the subject of several excellent monographs and review articles [2–4, 22, 31], thus only a brief historical perspective will be provided here highlighted by recent advances in the application of EPR toward the study of biologically relevant Mn(II) complexes.

In work pioneered by the research group of Mildred Cohn [48–54] at the University of Pennsylvania, continuous-wave (CW) EPR spectroscopy was shown to be highly adept at probing the geometric and electronic structure of the Mn(II) ion present in ATP-dependent kinases. Through analysis of spectral changes upon the addition of natural abundance and isotopically labeled substrate, product, or inhibitor, they gained significant insight into substrate-induced active site rearrangements [51] and were able to propose models of the reaction transition state.

Cohn and Reed noted that interpretation of their data was made significantly easier by going to higher excitation frequencies (e.g., K-band [30 GHz] and Q-band [35 GHz]) as the spectra took on more first-order-like properties. This purifying effect results from the correspondingly high applied magnetic field which increases the electron Zeeman splitting and attenuates the ability of ZFS and hyperfine interactions to mix wave functions, a principle that is one of the foundations of the multifrequency approach. Cohn and Reed were also among the first investigators to appreciate the “anisotropic magnetic interactions” that lead to the appearance of outer transition in spectra of frozen protein solutions. Unfortunately, these features manifested in CW EPR data only when the ZFS parameters were relatively large and suffered from little strain (as in single-crystal data; e.g., see refs. 44 and 46). Pulsed EPR studies of Mn(II)-containing systems, however, do not suffer from this limitation as this absorption-mode technique is sensitive to broad transitions that are difficult to detect via the field-modulated acquisition mode used in CW EPR spectroscopy. A noteworthy alternative to the typical field-modulated CW EPR experiment, which also gives absorptive EPR line shapes, is the method of rapid adiabatic passage (RAP) developed at Bell Telephone Laboratories by Weger and Feher and coworkers [55] and applied to the study of biological systems by Hoffman, Hyde, Peisach, Taylor, and others [56–60]. Furthermore, ESEEM and ENDOR spectroscopies can probe the small hyperfine couplings between the Mn center and nearby magnetic nuclei, which tend to get lost within the inhomogeneously broadened line shape of an electron spin transition [61, 62].

The EPR at multiple frequencies (MF EPR) approach is well illustrated by recent high-field studies that precisely determined ZFS parameters for MnSODs from a variety of organisms [42, 63, 64]. Both Mn- and Fe-containing SODs possess nearly identical first coordination spheres, yet Fe-substituted MnSOD and Mn-substituted FeSOD (Mn-(Fe)SOD) are both inactive. Intriguingly, there exists a cambialistic form of SOD that operates with either metal cofactor. Results from the 190–285 GHz CW EPR studies by Un and coworkers showed that the value of Mn(II) ZFS parameters could be correlated to activity. For example, mutation of a conserved glycine residue 1.1 nm from the Mn-binding site in cambialistic SOD resulted in a loss of Mn-dependent activity accompanied by ZFS values that are more similar to those found for Mn-(Fe)SOD [42]. This change in the electronic structure coincided with increased activity of the Fe-reconstituted form of the cambialistic SOD. Recent magnetic circular dichroism (MCD) spectroscopic and computational studies of Mn- and FeSOD confirmed the importance of these second coordination sphere amino acids as they participate in an extended H-bonding network that affects the protonation state of the axially coordinated solvent (shown in superscript in Eq. (1)) [65, 66]. This interaction is essential in tuning the redox potential of the Mn center for each half-reaction with superoxide.

Much research effort has been focused on obtaining ESEEM and ENDOR spectra of the various states of PSII [67–75]. While the Mn(II) oxidation state is likely not accessed during any of the so-called S states of the water oxida-

tion reaction² [76, 77], Mn(II) ions are necessary for the in vivo photoassembly of the Mn cluster [78]. During this process, an exogenous Mn(II) ion binds to an active site aspartate residue D1-Asp170 in Mn-depleted PSII [79], and is then photooxidized by the same light-harvesting machinery used for water oxidation. The cycle repeats as additional equivalents of Mn(II) as well as Ca²⁺ and Cl⁻ cofactors bind to yield the fully functional OEC. Interestingly, O₂ evolution measurements indicate that the presence of bicarbonate anion enhances the rate of photoassembly [80]. This effect can be rationalized as carboxylate coordination of the Mn(II) ion is known to stabilize the corresponding Mn(II) → Mn(III) oxidation potential from 1.5 to 0.5 V when bound to PSII [81]. Conveniently, this new potential is well within the range of 1.1 V accessible by the photooxidized active-site tyrosyl radical (Y₂[•]). Dismukes and coworkers [82] recently presented two-dimensional hyperfine sublevel correlation (2-D HYSCORE, a four-pulse ESEEM technique) spectroscopic results that quantitate the speciation of aqueous Mn(II) ions in the presence of ¹³C-labeled bicarbonate. These findings yielded a valuable spectroscopic signature for ¹³C hyperfine interactions due to exogenous carboxylate coordination to Mn(II) and open the door to analogous studies in Mn-depleted PSII.

Similarly, Mn(II) ions have been used to probe the mechanism of metal ion incorporation in the homodimeric diiron-dependent RNR [83–86]. Hendrich and coworkers used CW EPR data acquired at X- and Q-band frequencies to show that binding of a single Mn(II) ion to one of the domains of apo-RNR induced a significant allosteric event that prevented binding of an additional equivalent of Mn(II) to the other domain. Significantly, this work represented the first report wherein multifrequency spectral simulations were used to quantitate Mn(II) signals appearing in both perpendicular and parallel mode ($\Delta m_s = 0$) spectra [85].

Historically, ZFS parameters for Mn(II) centers have been used as an indicator of coordination number, where large magnitudes for D imply five-coordinate systems and smaller values tend to be representative of a manganous ion in near-cubic geometries (e.g., O_h or T_d; see Sect. 2). However, a recent series of Q-band (35 GHz) RAP CW EPR, echo-detected field-swept (ED-FS) EPR, pulsed and CW ENDOR spectroscopic studies on FosA, a manganese-dependent glutathione transferase, nicely illustrate that the identities of each ligand and its corresponding electronic structure play as much, if not more, a role in the determination of ZFS parameters [59, 87]. Indeed, EPR spectral changes incurred as different substrates (inhibitors) were bound to the Mn(II) active site of FosA were correlated to changes in both coordination number as well as the nature of the ligand field. Importantly, this data helped point to a possible molecular mechanism by which FosA helps bacteria subvert the effects of the broad-spectrum antibiotic fosfomycin.

² The Mn(II) oxidation has been invoked in the past as participating in early steps of the Kok cycle (S₀ or S₁); however, recent pulsed Q-band ENDOR spectra of PSII strongly suggest that Mn₄(III,III,III,IV) is the likely set of Mn oxidation states present in the S₀ state [77].

Many of the biosystems described above have been modeled by inorganic chemists and EPR spectroscopy serves as an essential tool in the evaluation of the electronic and geometric properties of these synthetic analogues [1, 88–90]. In particular, Mn(II):nucleotide adducts and other metal-bound small-molecule constructs (e.g., Mn(II) bound to synthetic RNA) have attracted much attention owing to the involvement of these species in crucial biochemical processes such as ATP hydrolysis [31], RNA sequence modification [33, 91], and cellular signaling. One of the most intensely studied of these systems is the HH ribozyme, a short self-cleaving fragment RNA motif involved in viroid RNA replication [92, 93]. Though home to numerous divalent metal binding sites, the role of these metals in the function of ribozymes is still under scrutiny. Certainly some of these metals are needed to aid in the proper folding of the RNA and others are implicated as taking part in the phosphodiester cleavage reaction. Biochemical and EPR spectroscopic studies carried out by DeRose and coworkers [92, 94] found that only one of these sites tightly binds its respective metal ion ($k_d \leq 10 \mu\text{M}$), and that this site must be populated for “catalytic” activity. However, all available spectroscopic evidence indirectly suggested that the high-affinity binding site exists between the N7 of a guanine residue (G10.1) and the phosphate oxygen of an adjacent adenine (A9), about 2.0 nm from the site of RNA cleavage [35, 92, 95–98]. Only recently has this tentative assignment been confirmed through ESEEM spectroscopic measurements of site-specific isotope labeling of the G10.1 nitrogens [99]. Herein, we report results from EPR spectroscopic experiments at multiple frequencies to study a set of simple nucleotide and RNA Mn(II) complexes. Spin Hamiltonian parameters derived from spectral simulations, as well as line narrowing and concomitant sensitivity enhancements for EPR at given frequencies, are discussed in terms of binding site disorder.

4 Materials and Methods

The University of California at Davis now operates several pulsed EPR spectrometers that employ X- to Ku- (8–18 GHz), Ka- (30 GHz), Q- (35 GHz), and D-band (130 GHz) excitation frequencies. At this CALEPR facility, ED-FS EPR, ENDOR, and ESEEM spectra at liquid-helium temperatures can be collected at each of the above frequencies. An accounting of the instrumentation available at CALEPR follows as well as a description of the methods used for data analysis. Conditions for sample preparation of a series of Mn(II)-containing systems used to exemplify these capabilities are also described.

X-Band. Perpendicularly polarized CW X-band spectra were acquired using a Bruker model ECS106 with a dual-mode cavity operating in TE_{102} mode. Temperature control was maintained with an Oxford Instruments model ESR900 helium flow cryostat coupled to an Oxford ITC 503 temperature controller. Pulsed X-band spectroscopy was performed using a laboratory-built spectrometer with 8–18 GHz excitation frequency capabilities that has been previously described [100].

Ka-Band. We have recently completed construction of a Ka-band EPR instrument that operates within a 1 GHz bandwidth (30.5–31.5 GHz) in conjunction with a GMW 1.4 T electromagnet and is diagrammed in Fig. 2. ED-FS EPR as well as 2- and 3-pulse ESEEM spectra can be acquired with deadtimes of about 100 ns. The instrument is administered by Labview 6.0 software using an 8-channel (400 MHz, 2.5 ns resolution) pulse programmer (Tektronix DG2030). Microwave power is directed through the spectrometer via copper waveguide (WR28). The low-power tuning arm microwaves are produced by a varactor tunable Gunn oscillator (Quinstar Technology). Higher-power microwaves are created in the pulse arm by a second Gunn oscillator (Spacek Labs) wherein the frequency can be mechanically tuned over a 1 GHz bandwidth. Short pulses are formed by a high-speed PIN switch (Millitech) and amplified to high power via a 100 W TWT amplifier (NEC Inc.). The minimum pulse widths are of about

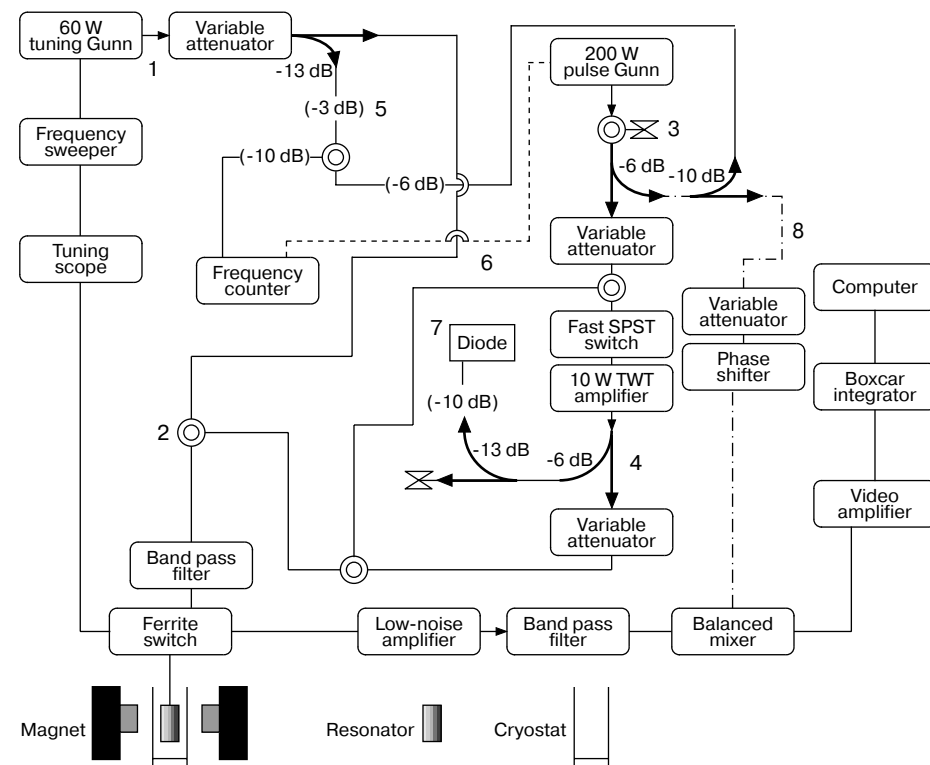


Fig. 2. Schematic of the homebuilt pulsed Ka-band microwave bridge. The numbered regions represent common components throughout the bridge and are as follows: (1) isolator, (2) mechanical 3-way switch (SPDT), (3) terminator, (4) directional coupler with labeled attenuation, (5) fixed attenuator with labeled attenuation, (6) dotted line representing the frequency and phase lock loop from the frequency counter to the high-power pulse Gunn, (7) diode for monitoring pulse lengths and shapes, (8) reference arm.

10 ns. Microwave circulation into and out of the sample cavity is managed by a five-junction TTL-driven ferrite switch (EMS Technologies). Transmission energy may be directed into high-power terminators in the first two ferrite ports, or switched directly into the cavity. Ambient noise from CW TWTA is thereby minimized during echo detection. Moreover, the ferrite device is employed to protect bridge receiver circuitry, serving as a defense gate by terminating high-power microwave pulse reflections from cavity, switching only to the output port for expected echo signal. Along the receiver arm, the output echo signal from the ferrite switch is first directed into a low-noise microwave preamplifier (Spacek Labs) and then to a band pass filter (Spacek Labs) to remove video frequency transient signals. Following these stages, the echo signal is passed to a homodyne balanced mixer (Spacek Labs). The output of the mixer can be further amplified with a multistage external video amplifier (Ortec). The spin echo signals are then integrated and averaged with a gated integrator and boxcar averager (Stanford Research model 250). The signal is then passed via an ADC card (National Instruments model PCI-6023E) to a personal computer.

The cavity resonator is a homebuilt thick-walled brass cylindrical cavity that operates in the TE_{011} mode. Frequency tuning of the resonator is achieved via a movable bottom plate. Coupling to the resonator was accomplished through a brass tunable short that was centered in the bottom of copper WR28 waveguide. Both the movable end plate and tunable short are mechanically connected to the top of the probe through thin-wall stainless steel tubing. The probe was machined to fit into a Janis model SVT cryostat for all experiments.

D-Band. The D-band pulsed spectrometer is a laboratory-constructed instrument, using a commercial 130 GHz microwave bridge and a probe with a TE_{011} mode cylindrical resonant cavity, both designed and manufactured by HF EPR Instruments, Inc. (V. Krymov, New York) [101]. The spectrometer uses an Oxford wide-bore 300 MHz nuclear magnetic resonance (NMR) superconducting magnet charged to a field of 4.64 T, close to $g = 2$ at 130 GHz. A 900 G sweep range about the field set by the superconducting magnet is provided for by a water-cooled copper solenoid that is inserted between the magnet cryostat and the sample cryostat. The solenoid is made of AWG18 rectangular magnet wire and controlled by an Agilent 6675A programmable power supply. Microwave and radiofrequency pulses are controlled by a Tektronix DG2030 word generator, and data acquisition is performed using a Tektronix 5054B Digital Phosphor Oscilloscope operating in fast frame acquisition mode. Sample temperature control is achieved using an Oxford liquid-helium cryostat in conjunction with an Oxford Instruments ITC. Computer control is provided by laboratory-written software using National Instruments LabVIEW 8.0. Samples are contained in quartz capillaries with 0.6 mm OD, 0.5 ID with about 1 μ l of the sample inside the EPR cavity.

Data Analysis. The relative signal-to-noise ratio (S/N) for each instrument was calculated from a single ED-FS EPR spectrum (20 echoes averaged per data point) of a 10 μ M solution of Mn(II)Cl₂ in water and 20% ethylene glycol (v/v). “Noise” was determined by rms average peak-to-peak amplitude of

baseline noise in the high-field wing of the spectrum. “Signal” was determined by the maximum amplitude of a central transition peak. S/N for each instrument is as follows: X-band, 8; Ka-band, 21; D-band, 38. Spectral simulations were performed by diagonalizing the spin Hamiltonian given in Eq. (2) in the rotating frame using the Easyspin package developed by Stephen Stoll at ETH-Zurich (<http://www.easyspin.ethz.ch/>) [102, 103] for MatLab 6.1 software (The Mathworks, Inc.).

Sample preparation. All buffers, reagents, and nucleotides (Sigma) were of the highest purity available and used without further purification, except as noted. Guanosine 5'-monophosphate (GMP) and adenosine 5'-triphosphate (ATP) samples contained 5 mM nucleotide – 1.0 mM Mn(II)Cl₂ and 1.2 mM nucleotide – 1.0 mM Mn(II)Cl₂, respectively. Mn(II)EDTA was prepared with a slight excess of chelator. All samples were buffered to pH 7.0 using 10 mM sodium dimethylarsino oxide (sodium cacodylate) and cryoprotected with 20% ethylene glycol before being immediately (<20 s) frozen in liquid nitrogen. The 34-nucleotide RNA enzyme (Dharmacon Research Inc., Boulder, CO) and 13-nucleotide DNA substrate strands (Integrated DNA Technologies) were purified as described previously [92, 94, 104]. HH hybrids were formed by adding equimolar amounts of enzyme and substrate oligomers, heating to 90 °C for 3 min, and then cooled slowly to room temperature. Mn(II)Cl₂ (American Analytical, Ultrapure grade) and ethylene glycol were added following hybrid formation.

5 Results and Analysis

CW X-Band (9.7 GHz) Studies. The low-temperature (6 K) X-band CW EPR spectra of Mn(II) in H₂O, with GMP, with ATP, and bound to the HH/DNA hybrid (MnHH) (Fig. 3) all exhibit the six-line pattern centered at $g = 2.00$ that is attributed to the hyperfine-split central transition ($|+1/2\rangle \leftrightarrow |-1/2\rangle$) of high-spin ($S = 5/2$) ⁵⁵Mn(II) complexes. Closer inspection reveals subtle differences in the breadth and intensity of several spectral features. Most notably the highest field resonance (ca. 3700 G) for Mn(II)ATP is significantly broader than that for the other three species. Also, the intensity of the forbidden transitions (indicated by the asterisks in Fig. 3) relative to that of the allowed central transition is greatest in the spectrum of Mn(II)ATP. The following relation predicts the magnitude of this ratio as a function of D and the electron Zeeman splitting [105].

$$\frac{I_{\text{forb}}}{I_{\text{allowed}}} = \left(\frac{D \sin 2\theta}{g\beta B_0} \right)^2 \left(64 \left(\frac{35}{4} - m_l^2 - m_l \right) \right). \quad (4)$$

Qualitatively, this behavior suggests that the axial ZFS parameter D is largest for the Mn(II)ATP adduct and approximately equivalent for the other three adducts. Interestingly, while all data were acquired under identical conditions, the spectral line width for MnHH is noticeably narrower than for any other species.

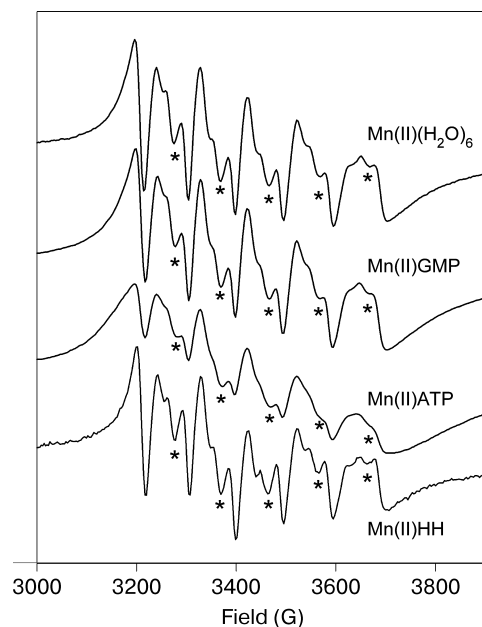


Fig. 3. Normalized CW X-band spectra of Mn(II) in H₂O, 1:5 mixture of Mn(II) and GMP, 1:1.2 mixture of Mn(II) and ATP, and 1:1.2 mixture of Mn(II) and HH ribozyme. Instrument conditions: $\nu_{\text{MW}} = 9.68\text{--}9.70$ GHz; time constant, 82 ms; conversion time, 41 ms; modulation frequency, 100 kHz; modulation amplitude, 1 G.

This may indicate that the ligand field around the Mn(II) ion bound to the macromolecular ribozyme is much less disordered than that for the nucleotide adducts in solution.

In an attempt to observe the outer transitions and thus get an independent estimate of the ZFS parameters, additional CW EPR spectra were acquired under high-power and high-receiver gain conditions [46]. Unfortunately, no such features were observed (data not shown) suggesting that D is much less than a quantum of microwave energy at X-band ($D \ll g\beta B_0$) or that the ZFS parameters are significantly distributed due sample inhomogeneity (D -strain).

Pulsed EPR Studies. Normalized ED-FS EPR data acquired at 9.4 GHz and 6 K for the four Mn(II) complexes are compared on the left-hand side of Fig. 4. All spectra appear as a sextet of rather broad (full width at half-maximum of about 50 G) peaks centered at $g = 2.00$ again resulting from the ⁵⁵Mn hyperfine-split central EPR transition. This feature sits atop a broad Gaussian-shaped absorption attributed to the four unresolved underlying outer transitions, a pattern that is basically replicated for the data collected at 30 and 130 GHz (Fig. 4). However, with increasing excitation frequency, the manifolds of outer transitions become dispersed over a larger field range. The central transitions, meanwhile, remain intense and become narrower due to the mitigation of second-order line broadening from ZFS contributions. The insets in Fig. 4a and b afford

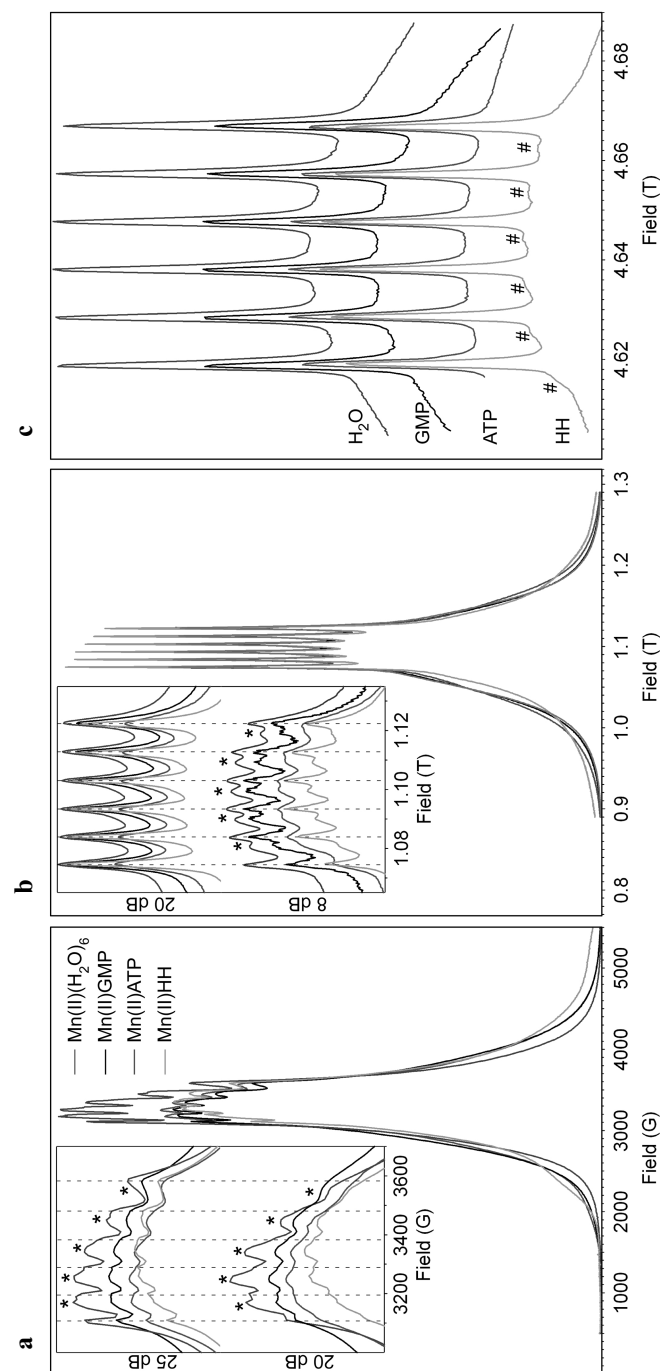


Fig. 4. Normalized electron spin ED-FS EPR spectra of Mn(II)-containing samples (described in legend of Fig. 3) acquired at 6.0 K using X-band (a), Ka-band (b), and D-band (c) frequencies. Insets in panels a and b highlight the sextet of EPR transitions between the central m_s manifold ($|+1/2\rangle \leftrightarrow |-1/2\rangle$) and illustrate the effect increased microwave power B_1 has on the intensity of the forbidden transitions (indicated by the asterisks). Instrumental conditions were the following. X-band: $\nu_{\text{MW}} = 9.36$ GHz; repetition time, 8 ms; sweep width, 3500 G; $H = 10$ G; 10 echoes per point; $t_{\text{acq}} = 15$ ns; $t_{\text{e}} = 30$ ns; $\tau = 210$ ns. Ka-band: $\nu_{\text{MW}} = 30.758$ GHz; repetition time, 5 ms; sweep width, 4000 G; $H = 3$ G; 10 echoes per point; $t_{\text{acq}} = 30$ ns; $t_{\text{e}} = 60$ ns; $\tau = 220$ ns. D-band: $\nu_{\text{MW}} = 130$ GHz; repetition time, 2 ms; $H = 3$ G; 100 echoes per point; $t_{\text{acq}} = 50$ ns; $t_{\text{e}} = 100$ ns; $\tau = 300$ ns.

a closer examination of the central transitions and illustrate the power dependence of the forbidden transitions (indicated by the asterisks). While the X-band data are too encumbered by the presence of forbidden transitions to visually distinguish any meaningful properties of the central transitions, the spectra taken using a frequency of 30 GHz are nearly free of any forbidden transition intensity in this region, and only by increasing the power from 136 to 343 mW do they become significantly intense. As with the results from the corresponding CW EPR experiments, the intensity of the forbidden transitions is greatest for Mn(II)ATP, again suggesting that this species has the largest ZFS of the four studied. Further evidence to this effect is gained by observing that the total line width of the set of outer transitions is broadest for Mn(II)ATP at all three frequencies.

D-band EPR data for aqueous Mn(II) and both Mn:nucleotide adducts are completely devoid of any forbidden transition intensity (Fig. 4c) at all powers used (data not shown). This is as expected since D would have to be on the order of 1200 MHz to appreciably contribute forbidden transition intensity given the large value of the electron Zeeman term (Eq. (4)). Very surprising, however, is the presence of what appear to be forbidden transitions in the D-band spectrum of MnHH (indicated by the # symbols in Fig. 4). Alternatively, these features could be attributed to resolved members of the hyperfine-split outer transitions. This latter explanation is more plausible due to the appearance of a sixth peak to the low-field side of the first member of the central transition, as opposed to five expected peaks for forbidden transitions (Sect. 2). This observation suggests that binding of a Mn(II) ion to the high-affinity site in the ribozyme does not distort the ligand field to induce exceedingly large ZFS parameters, but rather that the distribution in Mn(II) ZFS is unusually narrow (see below).

Simulations of the CW EPR and pulsed MF EPR data for all four systems were performed by direct diagonalization of the effective spin Hamiltonian given in Eq. (2) in the $|m_s, m_l\rangle$ basis (see examples in Fig. 5). With regards to the CW EPR spectra, the quality of our fits was judged based on the forbidden-to-allowed transition intensity ratio (Eq. (4)) and the appearance of the highest-field feature, which is known to be sensitive to the degree of rhombicity or E/D ratio in the ZFS values [31, 38]. Unfortunately, obtaining a unique set of parameters that precisely fit both pulsed and CW EPR data is not yet possible owing to several factors: (i) inability to account for B_1 -dependence of forbidden transition intensity³; (ii) simulations of pulsed EPR data give artificially intense outer transitions due to the fact that the optimal pulse length t_p used to tip magnetization by 90° and 180° is a function of the corresponding m_s quantum number, a property not accounted for in Easyspin [41]; and (iii) empirical differences in spectral line width as a function of the m_s quantum numbers of the donor and

³ We acknowledge the contribution by Coffino and Peisach [39] to this issue whereby a time-dependent perturbation that is a function of B_1 is added to the effective spin Hamiltonian. However, as some systems in the present study possess ZFS constants on the order of the electron Zeeman term (e.g., Mn(II)EDTA) we chose to employ a direct diagonalization approach exclusively.

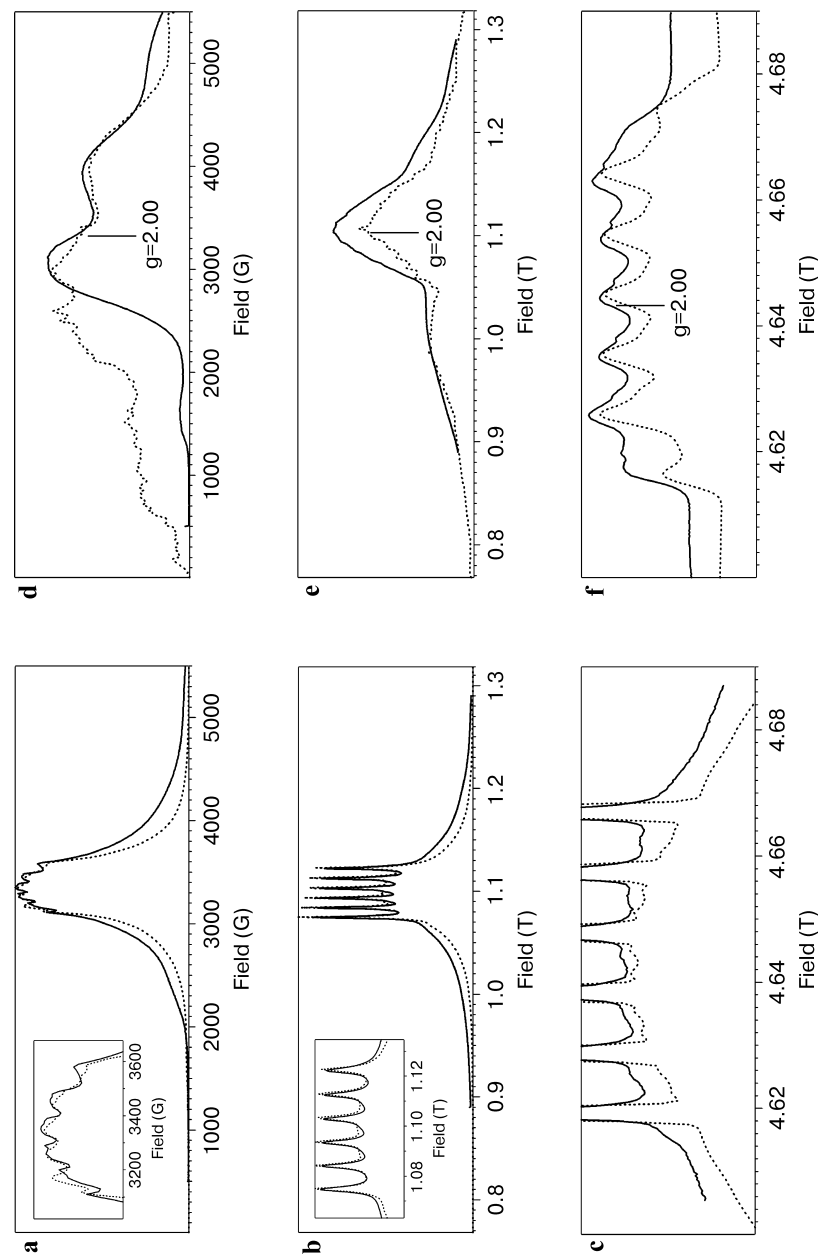


Fig. 5. ED-FS EPR spectra (solid lines) and spectral simulations (dotted lines) of MnHH (a–c) and Mn(II)EDTA (d–f) collected at 9.4 (a, d), 30.8 (b, e), and 130 GHz (c, f) frequencies. Instrument parameters are identical to those described in the legend of Fig. 4.

acceptor spin levels taking part in the EPR transition [40, 106]. In spite of these inherent limitations, satisfactory simulations were achieved and the best-fit parameters are summarized in Table 1 and compared to literature values for relevant Mn(II):nucleotide adducts and proteins.

On the whole, our simulated ZFS parameters are in fair agreement with those found in the literature for similar complexes. The minor disparity between the magnitudes of D for $[\text{Mn(II)(H}_2\text{O)}_6]^{2+}$ likely results from a difference in glassing agent [39, 40]. Indeed, Halkides et al. [107] showed that glycerol, used in previous studies, can displace water ligands from Mn(II) centers, indicating that our choice of a much lower concentration of ethylene glycol (20% vs. 50% [v/v], respectively) may result in a more representative spectrum of $[\text{Mn(II)(H}_2\text{O)}_6]^{2+}$. More significant, however, is the difference between the two sets of parameters for Mn(II)ATP. Again, this could result from our use of a different glassing agent. Intriguingly, satisfactory fits for the MnHH data did not require the use of a large axial ZFS parameter as was perhaps implied by the presence of fine structure in the 130 GHz spectrum (Fig. 4c). Rather, very narrow line widths – 25% smaller than that used to simulate the D-band spectrum of $[\text{Mn(II)(H}_2\text{O)}_6]^{2+}$ – and minimal D - and E -strain were required (Fig. 5a–c). The implications of these findings are discussed below.

The breadth of each central transition (full width at half-maximum) for the set of Mn(II) adducts studied is presented in Table 2. One notices that the line width of the MnHH is significantly narrower (20–30%) than that for any other Mn(II) species studied, just as was seen in the CW EPR data discussed above (Fig. 3). These spectral line widths are dominated by two effects: (i) broadening

Table 2. Spectral line widths of X-, Ka-, and D-band ED-FS EPR spectra.

| Peak | Full width at half-maximum (G) for: | | | | | | | | | | | |
|------|-------------------------------------|----|----|-------|----|----|-------|----|----|------|----|----|
| | $[\text{Mn(H}_2\text{O)}_6]^{2+}$ | | | MnATP | | | MnGMP | | | MnHH | | |
| | X | Ka | D | X | Ka | D | X | Ka | D | X | Ka | D |
| 1 | >30 | 22 | 16 | >30 | 30 | 14 | >30 | 23 | 15 | >30 | 20 | 13 |
| 2 | >30 | 22 | 16 | >30 | 29 | 14 | >30 | 21 | 14 | >30 | 19 | 12 |
| 3 | >30 | 22 | 15 | >30 | 28 | 14 | >30 | 22 | 14 | >30 | 19 | 11 |
| 4 | >30 | 21 | 16 | >30 | 29 | 14 | >30 | 22 | 14 | >30 | 20 | 11 |
| 5 | >30 | 22 | 16 | >30 | 35 | 14 | >30 | 25 | 15 | >30 | 21 | 11 |
| 6 | >30 | 27 | 17 | >30 | 35 | 15 | >30 | 30 | 16 | >30 | 20 | 13 |

induced by the frequency bandwidth of the set of excitation pulses (i.e., spectral resolution) and (ii) inhomogeneous broadening due to ligand hyperfine interactions, ZFS (and strain), and variance in the ligand conformation about the Mn(II) center. The former rationale cannot be affecting the line width in the X-, Ka-, and D-band data sets as the inversion pulse used in each experiment has a significantly more narrow bandwidth (11.9, 2.0 and 3.5 G, respectively) than that measured (Table 2). Yet ZFS can only contribute to broadening of the central transitions to second order and any significant contribution would be minimized by going to higher field. This leaves only the degree of disorder in the ligand field as the dominant factor contributing to the magnitude of the line width for the central transitions in the D-band spectral data. Thus with respect to MnHH, these findings imply that the metal center exists in a highly ordered ligand conformation. This conclusion is a bit surprising given the rather modest dissociation constant ($k_d \leq 10 \mu\text{M}$) measured for the high-affinity metal binding site [92], as well as the fact that ^2H ESEEM studies of MnHH have established the presence of four water ligands bound to the Mn(II) center [104, 108]. One might assume that these factors would suggest that the ligand sphere about the metal center is rapidly changing, leading to a heterogeneous distribution of active site conformations. Nonetheless, earlier $^{14}\text{N}/^{15}\text{N}$ ESEEM studies took note of the fact that data from MnHH was much more resolved than that for Mn(II)GMP in water, suggesting a much more ordered system is indeed present in the ribozyme. This behavior must be attributed to the ability of the macromolecular RNA molecule to sequester the metal binding site away from bulk solvent, thus precluding facile ligand exchange and exerting absolute control over the coordination environment of this essential metal center. Recent results from ESEEM experiments performed by our laboratory using site-specifically labeled RNA have precisely identified this binding site as the A9/G10.1 site [99]. The sole nitrogenous RNA-based ligand identified in earlier studies [94, 109] is for the first time conclusively attributed to the N7 from G10.1. Another oxygen atom, likely from the phosphate 5' to the adjacent adenosine (A9) also binds, making the pseudo-oc-

Table 1. ZFS parameters for various Mn(II)-protein and/or nucleotide complexes.

| Complex | D (MHz) | E (MHz) | Reference or source |
|--|-----------|-----------|---------------------|
| $[\text{Mn(II)(H}_2\text{O)}_6]^{2+}$ with 50% glycerol | 550 | 55 | 106 |
| $[\text{Mn(II)(H}_2\text{O)}_6]^{2+}$ | 430 | 140 | 39 |
| $[\text{Mn(II)(H}_2\text{O)}_6]^{2+}$ with 20% ethylene glycol | 610 | 0 | this study |
| Mn(II)ATP | 580–670 | 0–160 | 51 |
| Mn(II)ATP | 1050 | 300 | this study |
| Mn(II)GMP | 420 | 100 | this study |
| Mn(II)EDTA | 1500 | 500 | 110 |
| Mn(II)EDTA | 3000 | 300 | this study |
| HH ribozyme (1 M NaCl) | 560 | | 35 |
| HH ribozyme (1 M NaCl) | 550–600 | 130 | this study |
| FosA | 3150 | 600 | 87 |
| FosA + phosphonoformate | 2700 | 90 | 87 |
| FosA + fosfomycin | 7050 | 660 | 87 |
| Pyruvate kinase + ATP | 3640 | 1210 | 31 |
| Creatine kinase + ADP | 840 | 0 | 31 |
| Myosin1 + ADP | 1090 | 360 | 31 |
| Oxalate decarboxylase | 1120 | | 17 |

tahedral Mn(II) ion coordinatively saturated and rationalizing the relatively small ZFS constants determined from spectral simulation (Table 1).

As an interesting final example of the MF EPR approach applied to Mn(II)-containing systems, we present pulsed EPR data for Mn(II) bound to the hexadentate ligand EDTA (Fig. 5) at X-, Ka-, and D-band frequencies. Strikingly, these data look nothing like the other spectra shown above as no ^{55}Mn hyperfine structure is visible in the X-band data and instead extremely broad features appear throughout the spectral range (Fig. 5a and d). Reed and Markham [31] observed that the X-band CW EPR spectrum of Mn(II)EDTA is broadened beyond detection and that only by increasing the field and frequency could even the central transitions be seen. Upon comparison of the pulsed EPR spectra at all three frequencies, one notes that the apparent g -values for these broad features can be sensitive to the magnitude of the excitation frequency (when D is nonzero), consistent with their assignment to the outer transitions. The ZFS parameters derived from spectral simulations are significantly different from those previously determined [110] and are noticeably larger than those for any other system studied in this report. Usually such large values imply that the Mn(II) center is no longer in a pseudo-octahedral ligand field and is likely pentacoordinate [42, 44, 87] or some highly distorted tetrahedron [111]. However, NMR and X-ray crystallographic results clearly indicate that Mn(II)EDTA is seven-coordinate with a water ligand occupying an apical position [112, 113]. The simulated EPR data presented in Fig. 5 were achieved using a near-axial ZFS tensor ($E/D = 0.1$), a finding supported by the axial geometry observed in the crystal structure of the Mn(II)EDTA complex [112]. As this species serves to calibrate our water-counting measurements via ESEEM spectroscopy, the MF EPR spectroscopic characterization of Mn(II)EDTA presented here is essential to extending these types of studies to higher frequencies [98, 114].

In conclusion, the MF EPR approach is not only useful in determining spin Hamiltonian parameters for paramagnetic systems (Eq. (2)) but may also provide clues as the degree of homogeneity associated with the binding site of the metal cofactor. By going to higher field and frequency, the individual spin transition manifolds become more isolated, greatly simplifying results from the application of advanced pulsed techniques such as ENDOR [115–117]. As described in Sect. 4, high-field experiments are more sensitive and require much less sample (about 1 μl for D-band) than their low-frequency counterparts, minimizing the expense of isotopically labeled sample preparations.

Acknowledgments

This paper is dedicated to George Feher on the occasion of his 82nd birthday, and in recognition of the 50th anniversary of the invention of ENDOR spectroscopy. We thank V. Krymov for many useful discussions and advice concerning the installation of the D-band spectrometer. The work conducted in the laboratory of V.J.D. is supported by the NIH (GM 58096) and NSF (CHE 0111696). R.D.B. acknowledges the continuing support of the NIH (GM 48242); and GM

61211 for funding the construction of the Ka-band spectrometer. The work of M.B. was supported by Swiss National Science Foundation Grant 8220-067593.

References

1. Wieghardt K.: *Angew. Chem.* **101**, 1179–1198 (1989)
2. Pecoraro V.L. (ed.): *Manganese Redox Enzymes*. Weinheim: VCH 1992.
3. Yocum C.F., Pecoraro V.L.: *Curr. Opin. Chem. Biol.* **3**, 182–187 (1999)
4. Sigel A., Sigel H. (eds.): *Manganese and Its Role in Biological Processes*. Metal Ions in Biological Systems, vol. 37. New York: Marcel Dekker 2000.
5. Miller A.-F., Sorkin D.L.: *Comments Mol. Cell. Biophys.* **9**, 1–48 (1997)
6. Jackson T.A., Yikilmaz E., Miller A.-F., Brunold T.C.: *J. Am. Chem. Soc.* **125**, 8348–8363 (2003)
7. Miller A.-F., Padmakumar K., Sorkin D.L., Karapetian A., Vance C.K.: *J. Inorg. Biochem.* **93**, 71–83 (2003)
8. Miller A.-F.: *Curr. Opin. Chem. Biol.* **8**, 162–168 (2004)
9. Jackson T.A., Brunold T.C.: *Acc. Chem. Res.* **37**, 461–470 (2004)
10. Gold M.H., Glenn J.K.: *Methods Enzymol.* **161**, 258–264 (1988)
11. van Aken B., Agathos S.N.: *Appl. Microbiol. Biotechnol.* **58**, 345–351 (2002)
12. Sundaramoorthy M., Youngs H.L., Gold M.H., Poulos T.L.: *Biochemistry* **44**, 6463–6470 (2005)
13. Su C., Sahlin M., Oliw E.H.: *Adv. Exp. Med. Biol.* **507**, 171–176 (2002)
14. Oliw E.H.: *Prostaglandins Other Lipid Mediators* **68–69**, 313–323 (2002)
15. Gaffney B.J., Su C., Oliw E.H.: *Appl. Magn. Reson.* **21**, 411–422 (2001)
16. Su C., Oliw E.H.: *J. Biol. Chem.* **273**, 13072–13079 (1998)
17. Chang C.H., Svedruzic D., Ozarowski A., Walker L., Yeagle G., Britt R.D., Angerhofer A., Richards N.G.J.: *J. Biol. Chem.* **279**, 52840–52849 (2004)
18. Tanner A., Bowater L., Fairhurst S.A., Bornemann S.: *J. Biol. Chem.* **276**, 43627–43634 (2001)
19. Emerson J.P., Wagner M.L., Reynolds M.F., Que L. Jr., Sadowsky M.J., Wackett L.P.: *J. Biol. Inorg. Chem.* **10**, 751–760 (2005)
20. Que L. Jr., Reynolds M.F. in: *Manganese and Its Role in Biological Processes*. Metal Ions in Biological Systems, vol. 37 (Sigel A., Sigel H., eds.) 505–525. New York: Marcel Dekker 2000.
21. Whiting A.K., Boldt Y.R., Hendrich M.P., Wackett L.P., Que L. Jr.: *Biochemistry* **35**, 160–170 (1996)
22. Dismukes G.C.: *Chem. Rev.* **96**, 2909–2926 (1996)
23. Khangulov S.V., Barynin V.V., Melik-Adamyany V.R., Grebenko A.I., Voevodskaya N.V., Blyumenfel'd L.A., Dobryakov S.N., Il'yasova V.B.: *Bioorg. Khim.* **12**, 741–748 (1986)
24. Khangulov S.V., Barynin V.V., Voevodskaya N.V., Grebenko A.I.: *Biochim. Biophys. Acta* **1020**, 305–310 (1990)
25. Yoder D.W., Hwang J., Penner-Hahn J.E. in: *Manganese and Its Role in Biological Processes*. Metal Ions in Biological Systems, vol. 37 (Sigel A., Sigel H., eds.) 527–557. New York: Marcel Dekker 2000.
26. Barynin V.V., Whittaker M.M., Antonyuk S.V., Lamzin V.S., Harrison P.M., Artymiuk P.J., Whittaker J.W.: *Structure* **9**, 725–738 (2001)
27. Willing A., Follmann H., Auling G.: *Eur. J. Biochem.* **170**, 603–611 (1988)
28. Stubbe J.: *Proc. Natl. Acad. Sci. USA* **95**, 2723–2724 (1998)
29. Goussias C., Boussac A., Rutherford A.W.: *Philos. Trans. R. Soc. Lond. B* **357**, 1369–1381 (2002)
30. Barber J.Q.: *Rev. Biophys.* **36**, 71–89 (2003)
31. Reed G.H., Markham G.D.: *Biol. Magn. Reson.* **6**, 73–142 (1984)
32. Copik A.J., Nocek B.P., Swierczek S.I., Ruebush S., Jang S.B., Lu M., D'Souza V.M., Peters J.W., Bennett B., Holz R.C.: *Biochemistry*, **44**, 121–129 (2005)
33. DeRose V.J.: *Curr. Opin. Struct. Biol.* **13**, 317–324 (2003)
34. Hammann C., Lilley D.M.J.: *ChemBioChem* **3**, 690–700 (2002)
35. Morrissey S.R., Horton T.E., DeRose V.J.: *J. Am. Chem. Soc.* **122**, 3473–3481 (2000)
36. Dowsing R.D., Gibson J.F.: *J. Chem. Phys.* **50**, 294–303 (1969)
37. Abragam A., Bleaney B.: *Electron Paramagnetic Resonance of Transition Ions*. Oxford: Clarendon Press 1970.

38. Markham G.D., Rao B.D.N., Reed G.H.: *J. Magn. Reson.* **33**, 595–602 (1979)
39. Coffino A.R., Peisach J.: *J. Magn. Reson.* **111**, 127–134 (1996)
40. Tan X., Bernardo M., Thomann H., Scholes C.P.: *J. Chem. Phys.* **98**, 5147–5157 (1993)
41. Benetis P.N., Dave P.C., Goldfarb D.: *J. Magn. Reson.* **158**, 126–142 (2002)
42. Un S., Tabares L.C., Cortez N., Hiraoka B.Y., Yamakura F.: *J. Am. Chem. Soc.* **126**, 2720–2726 (2004)
43. LoBrutto R., Smithers G.W., Reed G.H., Orme-Johnson W.H., Tan S.L., Leigh J.S. Jr.: *Biochemistry* **25**, 5654–5660 (1986)
44. Sturgeon B.E., Ball J.A., Randall D.W., Britt R.D.: *J. Phys. Chem.* **98**, 12871–12883 (1994)
45. Duboc C., Astier-Perret V., Chen H., Pecaut J., Crabtree R.H., Brudvig G.W., Collomb M.-N.: *Inorg. Chim. Acta* **359**, 1541–1548 (2006)
46. Meirovitch E., Luz Z., Kalb A.J.: *J. Am. Chem. Soc.* **96**, 7538–7542 (1974)
47. Meirovitch E., Luz Z., Kalb A.J.: *J. Am. Chem. Soc.* **96**, 7542–7546 (1974)
48. Cohn M., Townsend J.: *Nature (London)* **173**, 1090–1091 (1954)
49. Jallon J.M., Cohn M.: *Biochim. Biophys. Acta* **222**, 542–545 (1970)
50. Reed G.H., Cohn M.: *J. Biol. Chem.* **245**, 662–664 (1970)
51. Reed G.H., Diefenbach H., Cohn M.: *J. Biol. Chem.* **247**, 3066–3072 (1972)
52. Reed G.H., Cohn M.: *J. Biol. Chem.* **248**, 6436–6442 (1973)
53. Buttlare D.H., Cohn M.: *J. Biol. Chem.* **249**, 5733–5740 (1974)
54. Wilson G.E. Jr., Cohn M.: *J. Biol. Chem.* **252**, 2004–2009 (1977)
55. Feher G.: *Phys. Rev.* **103**, 500–501 (1956)
56. Deigen M.F., Maevskii V.M., Zevin V.Y., Vitrikhovskii N.I.: *Radiospektrosk. Tverd. Tela* **1967** 317–320.
57. Seamonds B., Blumberg W.E., Peisach J.: *Biochim. Biophys. Acta* **263**, 507–514 (1972)
58. Mailer C., Taylor C.P.: *Biochim. Biophys. Acta* **322**, 195–203 (1973)
59. Smoukov S.K., Telser J., Bernat B.A., Rife C.L., Armstrong R.N., Hoffman B.M.: *J. Am. Chem. Soc.* **124**, 2318–2326 (2002)
60. Hyde J.S., Dalton L.: *Chem. Phys. Lett.* **16**, 568–572 (1972)
61. Britt R.D.: *Curr. Opin. Struct. Biol.* **3**, 774–779 (1993)
62. Britt R.D.: *ACS Symp. Ser.* **858**, 16–54 (2003)
63. Campbell K.A., Yikilmaz E., Grant C.V., Gregor W., Miller A.-F., Britt R.D.: *J. Am. Chem. Soc.* **121**, 4714–4715 (1999)
64. Tabares L.C., Cortez N., Agalidis I., Un S.: *J. Am. Chem. Soc.* **127**, 6039–6047 (2005)
65. Jackson T.A., Karapetian A., Miller A.-F., Brunold T.C.: *J. Am. Chem. Soc.* **126**, 12477–12491 (2004)
66. Jackson T.A., Xie J., Yikilmaz E., Miller A.-F., Brunold T.C.: *J. Am. Chem. Soc.* **124**, 10833–10845 (2002)
67. Hoganson C.W., Babcock G.T.: *Biochemistry* **31**, 11874–11880 (1992)
68. Britt R.D., Force D.A., Campbell K.A., Randall D.W., Gilchrist L.M., Clemens K.L., Gingell D.M., Peloquin J.M., Pham D.P., Debus R.J.: *ACS Symp. Ser.* **692**, 272–285 (1998)
69. Britt R.D., Campbell K.A., Peloquin J.M., Gilchrist M.L., Aznar C.P., Dicus M.M., Robblee J., Messinger J.: *Biochim. Biophys. Acta* **1655**, 158–171 (2004)
70. Debus R.J., Campbell K.A., Gregor W., Li Z.-L., Burnap R.L., Britt R.D.: *Biochemistry* **40**, 3690–3699 (2001)
71. Debus R.J., Aznar C., Campbell K.A., Gregor W., Diner B.A., Britt R.D.: *Biochemistry* **42**, 10600–10608 (2003)
72. Kim S.H., Gregor W., Peloquin J.M., Brynda M., Britt R.D.: *J. Am. Chem. Soc.* **126**, 7228–7237 (2004)
73. Clemens K.L., Force D.A., Britt R.D.: *J. Am. Chem. Soc.* **124**, 10921–10933 (2002)
74. Åhrling K.A., Evans M.C.W., Nugent J.H.A., Ball R.J., Pace R.J.: *Biochemistry* **45**, 7069–7082 (2006)
75. Evans M.C.W., Nugent J.H.A., Ball R.J., Muhiuddin I., Pace R.J.: *Biochemistry* **43**, 989–994 (2004)
76. Kok B., Forbush B., McGloin M.: *Photochem. Photobiol.* **11**, 457–475 (1970)
77. Kulik L.V., Epel B., Lubitz W., Messinger J.: *J. Am. Chem. Soc.* **127**, 2392–2393 (2005)
78. Zaltsman L., Ananyev G.M., Bruntrager E., Dismukes G.C.: *Biochemistry* **36**, 8914–8922 (1997)
79. Campbell K.A., Force D.A., Nixon P.J., Dole F., Diner B.A., Britt R.D.: *J. Am. Chem. Soc.* **122**, 3754–3761 (2000)
80. Baranov S.V., Tyryshkin A.M., Katz D., Dismukes G.C., Ananyev G.M., Klimov V.V.: *Biochemistry* **43**, 2070–2079 (2004)
81. Kozlov Y.N., Zharmukhamedov S.K., Tikhonov K.G., Dasgupta J., Kazakova A.A., Dismukes G.C., Klimov V.V.: *Phys. Chem. Chem. Phys.* **6**, 4905–4911 (2004)
82. Dasgupta J., Tyryshkin A.M., Kozlov Y.N., Klimov V.V., Dismukes G.C.: *J. Phys. Chem. B* **110**, 5099–5111 (2006)
83. Bollinger J.M. Jr., Edmondson D.E., Huynh B.H., Filley J., Norton J.R., Stubbe J.: *Science* **253**, 292–298 (1991)
84. Atta M., Nordlund P., Aaberg A., Eklund H., Fontecave M.: *J. Biol. Chem.* **267**, 20682–20688 (1992)
85. Pierce B.S., Elgren T.E., Hendrich M.P.: *J. Am. Chem. Soc.* **125**, 8748–8759 (2003)
86. Pierce B.S., Hendrich M.P.: *J. Am. Chem. Soc.* **127**, 3613–3623 (2005)
87. Walsby C.J., Telser J., Rigsby R.E., Armstrong R.N., Hoffman B.M.: *J. Am. Chem. Soc.* **127**, 8310–8319 (2005)
88. Law N.A., Caudle M.T., Pecoraro V.L.: *Adv. Inorg. Chem.* **46**, 305–440 (1998)
89. Pecoraro V.L., Gelasco A., Baldwin M.J.: *Adv. Chem. Ser.* **246**, 265–301 (1995)
90. Wu A.J., Penner-Hahn J.E., Pecoraro V.L.: *Chem. Rev.* **104**, 903–938 (2004)
91. Scott W.G.: *Curr. Opin. Chem. Biol.* **3**, 705–709 (1999)
92. Horton T.E., Clardy D.R., DeRose V.J.: *Biochemistry* **37**, 18094–18101 (1998)
93. Blount K.F., Uhlenbeck O.C.: *Annu. Rev. Biophys. Biomol. Struct.* **34**, 415–440 (2005)
94. Morrissey S.R., Horton T.E., Grant C.V., Hoogstraten C.G., Britt R.D., DeRose V.J.: *J. Am. Chem. Soc.* **121**, 9215–9218 (1999)
95. Scott W.G., Murray J.B., Arnold J.R.P., Stoddard B.L., Klug A.: *Science* **274**, 2065–2069 (1996)
96. Scott W.G., Murray J.B.: *Methods Enzymol.* **317**, 180–198 (2000)
97. Murray J.B., Scott W.G.: *J. Mol. Biol.* **296**, 33–41 (2000)
98. Murray J.B., Terwey D.P., Maloney L., Karpeisky A., Usman N., Beigelman L., Scott W.G.: *Cell* **92**, 665–673 (1998)
99. Vogt M., Lahiri S., Hoogstraten C., Britt R.D., DeRose V.J.: *J. Am. Chem. Soc.* (2006) in press.
100. Sturgeon B.E., Britt R.D.: *Rev. Sci. Instrum.* **63**, 2187–2192 (1992)
101. Dorlet P., Seibold S.A., Babcock G.T., Gerfen G.J., Smith W.L., Tsai A.-I., Un S.: *Biochemistry* **41**, 6107–6114 (2002)
102. Stoll S., Schweiger A.: *J. Magn. Reson.* **178**, 42–55 (2006)
103. Stoll S., Schweiger A.: *J. Magn. Reson.* **163**, 248–256 (2003)
104. Hoogstraten C.G., Grant C.V., Horton T.E., DeRose V.J., Britt R.D.: *J. Am. Chem. Soc.* **124**, 834–842 (2002)
105. Bleaney B., Rubins R.S.: *Proc. Phys. Soc. Lond.* **77**, 103–112 (1961)
106. Tan X., Bernardo M., Thomann H., Scholes C.P.: *J. Chem. Phys.* **102**, 2675–2690 (1995)
107. Halkides C.J., Farrar C.T., Singel D.J.: *J. Magn. Reson.* **134**, 142–153 (1998)
108. Hoogstraten C.G., Britt R.D.: *RNA* **8**, 252–260 (2002)
109. Schiemann O., Fritscher J., Kisseleva N., Sigurdsson S.T., Prisner T.F.: *ChemBioChem* **4**, 1057–1065 (2003)
110. More K.M., Eaton G.R., Eaton S.S.: *Inorg. Chem.* **25**, 2638–2646 (1986)
111. Wood R.M., Stucker D.M., Jones L.M., Lynch W.B., Misra S.K., Freed J.H.: *Inorg. Chem.* **38**, 5384–5388 (1999)
112. Richards S., Pedersen B., Silverton J.V., Hoard J.L.: *Inorg. Chem.* **3**, 27–33 (1964)
113. Zetter M.S., Grant M.W., Wood E.J., Dodgen H.W., Hunt J.P.: *Inorg. Chem.* **11**, 2701–2706 (1972)
114. McCracken J., Peisach J., Bhattacharyya L., Brewer F.: *Biochemistry* **30**, 4486–4491 (1991)
115. Eaton G.R., Eaton S.S.: *Appl. Magn. Reson.* **16**, 161–166 (1999)
116. Bar G., Bennati M., Nguyen H.-H.T., Ge J., Stubbe J., Griffin R.G.: *J. Am. Chem. Soc.* **123**, 3569–3576 (2001)
117. Andersson K.K., Schmidt P.P., Katterle B., Strand K.R., Palmer A.E., Lee S.-K., Solomon E.I., Graeslund A., Barra A.-L.: *J. Biol. Inorg. Chem.* **8**, 235–247 (2003)

Authors' address: R. David Britt, Department of Chemistry, University of California-Davis, One Shields Avenue, Davis, CA 95616, USA
E-mail: rdbritt@ucdavis.edu